AUTHOR QUERIES

AUTHOR PLEASE ANSWER ALL QUERIES

PLEASE NOTE: We cannot accept new source files as corrections for your article. If possible, please annotate the PDF proof we have sent you with your corrections and upload it via the Author Gateway. Alternatively, you may send us your corrections in list format. You may also upload revised graphics via the Author Gateway.

Carefully check the page proofs (and coordinate with all authors); additional changes or updates WILL NOT be accepted after the article is published online/print in its final form. Please check author names and affiliations, funding, as well as the overall article for any errors prior to sending in your author proof corrections.

1) **Please be aware that authors are required to pay overlength page charges ($230 per page) if the article is longer than 3 pages. If you cannot pay any or all of these charges please let us know. GRS Society members receive a discounted rate of $200 per page.**

2) **This pdf contains 2 proofs. The first half is the version that will appear on Xplore. The second half is the version that will appear in print. If you have any figures to print in color, they will be in color in both proofs.**

3) **The "Open Access" option for your article expires when the article is published on Xplore in an issue with page numbers. Articles in "Early Access" may be changed to Open Access. If you have not completed your electronic copyright form (ECF) and payment option please return to Scholar One "Transfer Center." In the Transfer Center you will click on "Manuscripts with Decisions" link. You will see your article details and under the "Actions" column click "Transfer Copyright." From the ECF it will direct you to the payment portal to select your payment options and then return to ECF for copyright submission.**

AQ:1 = Please check whether the edit made to the article title is appropriate.
AQ:2 = Please provide the expansions for ROC, BFGS, and AIRSAR.
AQ:3 = Please confirm or add details for any funding or financial support for the research of this article.
AQ:4 = Please confirm whether the corresponding author has been identified correctly.
AQ:5 = Please check and confirm whether the affiliation details of all the authors are correct as set.

Fusion of Evidences in Intensity Channels for Edge Detection in PolSAR Images

Anderson A. De Borba, Maurício Marengoni, and Alejandro C. Frery, *Senior Member, IEEE*

***Abstract*— Polarimetric synthetic aperture radar (PolSAR) sensors have reached an essential position in remote sensing. The images they provide have speckle noise, making their processing and analysis challenging tasks. We discuss an edge detection method based on the fusion of evidences obtained in the intensity channels hh, hv, and vv of PolSAR multilook images. The method consists of detecting transition points in the thinnest possible range of data that covers two regions using maximum likelihood under the Wishart distribution. The fusion methods used are: simple average, multiresolution discrete wavelet transform (MR-DWT), principal component analysis (PCA), ROC statistics, multiresolution stationary wavelet transform (MR-SWT), and a multiresolution method based on singular value decomposition (MR-SVD). A quantitative analysis suggests that PCA and MR-SVD provide the best results.**

***Index Terms*— Edge detection, fusion methods, maximum likelihood estimation, polarimetric synthetic aperture radar (PolSAR).**

I. Introduction

POLARIMETRIC synthetic aperture radar (PolSAR) has achieved an essential position in remote sensing. The data such sensors provide require specifically tailored signal processing techniques. Among such techniques, edge detection is one of the most important operations for extracting information. Edges are at a higher level of abstraction than mere data and, as such, provide relevant insights about the scene.

Among the available edge detection techniques for SAR and PolSAR images, it is worth mentioning: techniques based on denoising [1]–[4]; Markov random fields [5]; the deep learning approach [6] applied to segmentation and classification; and statistical techniques [7]–[9] applied in edge detection in PolSAR and SAR imagery.

This letter follows the statistical modeling approach using the techniques described in [7]–[9] to find edge evidences, followed by fusion processes [10], [11].

Instead of handling fully polarimetric data, we treat each intensity channel separately, obtain evidence of edges, and then produce a single estimator of the edge position. With this, we quantify the contribution each channel provides to the solution of the problem.

The Gambini Algorithm [12] is an attractive edge detection technique. It is local, as it finds evidence of an edge over a thin strip of data; it works with any model, which makes it suitable for SAR data; and it has shown better performance than other approaches. This algorithm consists in casting rays, and then finding the evidence of an edge in the ray by maximizing a value function. We use the total likelihood of two samples: one inside the edge and another outside the edge. Without loss of generality, we assume the complex scaled Wishart distribution for the fully polarimetric observations, from which Gamma laws stem for each intensity channel. The value function depends on the estimates that index such Gamma laws; and we estimate them by maximum likelihood.

The total likelihood function is nondifferentiable at most points, and classical methods have difficulties in finding its maximum. We used the generalized simulated annealing (GenSA) [13] method to solve this problem.

We discuss and compare six fusion methods: Simple average [10], multiresolution discrete wavelet (MR-DWT) [14], principal component analysis (PCA) [10], [14], ROC statistics [15], multiresolution stationary wavelet transform (MR-SWT) [14], [16], and multiresolution singular value decomposition (MR-SVD) [17].

The letter is structured as follows: Section II describes the models, Section III describes the edge detection, Section IV describes the approaches for fusing edge evidences, Section V presents the results, and in Section VI we discuss the results and outline future research directions.

II. Statistical Modeling for PolSAR Data

Multilooked fully polarimetric data follow the Wishart distribution with probability density function (PDF) defined by:

$$f_{\mathbf{Z}}(\mathbf{z};\,\Sigma,\,L) = \frac{L^{pL}|\mathbf{z}|^{L-p}}{|\Sigma|^{L}\Gamma_p(L)}\exp(-L\,\mathrm{tr}(\Sigma^{-1}\mathbf{z})) \qquad (1)$$

where $\mathbf{z}$ is a positive-definite Hermitian matrix, L is the number of looks, $\mathrm{tr}(\cdot)$ is the trace operator of a matrix, $\Gamma_p(L)$ is the multivariate Gamma function defined by $\Gamma_p(L) = \pi^{1/2p(p-1)}\prod_{i=0}^{p-1}\Gamma(L-i)$, and $\Gamma(\cdot)$ is the Gamma function. We used three $p = 3$ channels in this study. This situation is denoted by $\mathbf{Z} \sim W(\Sigma, L)$, which satisfies $E[\mathbf{Z}] = \Sigma$. This assumption usually holds for fully developed speckle but, since we will estimate L locally instead of considering the same number of looks for the whole image, we will in part take into account departures from such hypothesis.

Manuscript received March 24, 2020; revised July 12, 2020; accepted August 31, 2020. *(Corresponding author: Anderson A. De Borba.)*

Anderson A. De Borba is with the Department of Engenharia Elétrica e Computação, Universidade Presbiteriana Mackenzie (UPM), São Paulo 01302-907, Brazil, and also with IBMEC-SP, São Paulo 01419-002, Brazil (e-mail: anderson.aborba@professores.ibmec.edu.br).

Maurício Marengoni is with the Department of Engenharia Elétrica e Computação, Universidade Presbiteriana Mackenzie (UPM), São Paulo 01302-907, Brazil (e-mail: mauricio.marengoni@mackenzie.br).

Alejandro C. Frery is with the School of Mathematics and Statistics, Victoria University of Wellington, Wellington 6140, New Zealand (e-mail: alejandro.frery@vuw.ac.nz).

Color versions of one or more of the figures in this letter are available online at http://ieeexplore.ieee.org.

Digital Object Identifier 10.1109/LGRS.2020.3022511

Since we are interested in describing the information conveyed by parts of such matrix under the Wishart model, we assume that the distribution of each intensity channel is a Gamma law with PDF

$$f_Z(z;\mu,L)=\frac{L^L z^{L-1}}{\mu^L\Gamma(L)}\exp\{-Lz/\mu\},\quad z>0 \tag{2}$$

where $L>0$, and $\mu>0$ is the mean. The log-likelihood of the sample $\boldsymbol{z}=(z_1,\ldots,z_n)$ under this model is

$$\mathcal{L}(\mu,L;\boldsymbol{z})=n[L\ln(L/\mu)-\ln\Gamma(L)] +L\sum_{k=1}^{n}\ln z_k-\frac{L}{\mu}\sum_{k=1}^{n}z_k. \tag{3}$$

We obtain $(\widehat{\mu},\widehat{L})$, the maximum likelihood estimator (MLE) of (μ,L) based on $\boldsymbol{z}$, by maximizing (3) with the BFGS method [18]. We prefer optimization to solving $\nabla\ell=\mathbf{0}$ for improved numerical stability.

III. Edge Detection on a Single Data Strip

The Gambini algorithm estimates the point at which the properties of a sample change. It has been used with stochastic distances [9] and with the likelihood function [7], [8] for edge detection in SAR/PolSAR imagery. It can be adapted to any suitable measure of dissimilarity between two samples.

The algorithm starts by casting rays from a point inside the candidate region, e.g., the centroid. Data are collected around each ray to form the sample $\boldsymbol{z}=(z_1,z_2,\ldots,z_n)$, which is partitioned at position j

$$\boldsymbol{z}=(\underbrace{z_1,z_2,\ldots,z_j}_{\boldsymbol{z}_\mathrm{I}},\ \underbrace{z_{j+1},z_{j+2},\ldots,z_n}_{\boldsymbol{z}_\mathrm{E}}).$$

We assume two (possibly) different models for each partition: $\boldsymbol{Z}_\mathrm{I}\sim\Gamma(\mu_\mathrm{I},L_\mathrm{I})$, and $\boldsymbol{Z}_\mathrm{E}\sim\Gamma(\mu_\mathrm{E},L_\mathrm{E})$. We then estimate $(\mu_\mathrm{I},L_\mathrm{I})$ and $(\mu_\mathrm{E},L_\mathrm{E})$ with $\boldsymbol{z}_\mathrm{I}$ and $\boldsymbol{z}_\mathrm{E}$, respectively, by maximizing (3), and obtain $(\widehat{\mu}_\mathrm{I},\widehat{L}_\mathrm{I})$ and $(\widehat{\mu}_\mathrm{E},\widehat{L}_\mathrm{E})$.

We then compute the total log-likelihood of $\boldsymbol{z}_\mathrm{I}$ and $\boldsymbol{z}_\mathrm{E}$

$$\begin{aligned}\mathcal{L}(j;\widehat{\mu}_I,\widehat{L}_I,\widehat{\mu}_E,\widehat{L}_E)&=-\left(\frac{\widehat{L}_\mathrm{I}}{\widehat{\mu}_\mathrm{I}}\sum_{k=1}^{j}z_k+\frac{\widehat{L}_\mathrm{E}}{\widehat{\mu}_\mathrm{E}}\sum_{k=j+1}^{n}z_k\right)\\&\quad+j[\widehat{L}_\mathrm{I}\ln(\widehat{L}_\mathrm{I}/\widehat{\mu}_\mathrm{I})-\ln\Gamma(\widehat{L}_\mathrm{I})]+\widehat{L}_\mathrm{I}\sum_{k=1}^{j}\ln z_k\\&\quad+(n-j)[\widehat{L}_\mathrm{E}\ln(\widehat{L}_\mathrm{E}/\widehat{\mu}_\mathrm{E})-\ln\Gamma(\widehat{L}_\mathrm{E})]+\widehat{L}_\mathrm{E}\sum_{k=j+1}^{n}\ln z_k.\end{aligned} \tag{4}$$

and the estimate of the edge position on the ray is the coordinate $\widehat{j}$ which maximizes it.

Algorithm 1 is the pseudocode of the basic edge detection with the Gambini Algorithm. We found that 100 rays is a good compromise between spatial continuity and computational load. Also, $\min_s$ is the minimum sample size.

In our implementation, we replace the exhaustive sequential search (the innermost **for** loop) by GenSA [13].

Algorithm 1 Gambini Algorithm for Intensity Channels

Data: n_c intensity channels, interior point, number of rays
Result: n_c binary images with evidences of edges
for *each band* $1\le c\le n_c$ **do**
  for *each ray passing through the interior point* **do**
    $\boldsymbol{z}=(z_1,z_2,\ldots,z_n)\leftarrow$ data collected around the ray;
    for *each* $\min_s\le j\le n-\min_s$ **do**
      Partition the sample as $\boldsymbol{z}_\mathrm{I}=(z_{\min_s},\ldots,z_j)$ and $\boldsymbol{z}_\mathrm{E}=(z_{j+1},\ldots,z_{n-\min_s})$;
      Compute $(\widehat{\mu}_\mathrm{I},\widehat{L}_\mathrm{I})$ with $\boldsymbol{z}_\mathrm{I}$, and $(\widehat{\mu}_\mathrm{E},\widehat{L}_\mathrm{E})$ with $\boldsymbol{z}_\mathrm{E}$;
      Compute the total log-likelihood at j as $\mathcal{L}(j;\widehat{\mu}_I,\widehat{L}_I,\widehat{\mu}_E,\widehat{L}_E)$;
    end
    $\widehat{j}\leftarrow$ the value of j which maximizes the total log-likelihood function;
    return $(\widehat{x},\widehat{y})$, the coordinates of each $\widehat{j}$;
  end
  return the binary image $\widehat{\boldsymbol{J}}_c$ with 1 at every $(\widehat{x},\widehat{y})$, and 0 otherwise.
end

IV. Fusion of Evidences

Assume we have n_c binary images $\{\widehat{\boldsymbol{J}}_c\}_{1\le c\le n_c}$ in which 1 denotes an estimate of edge and 0 otherwise. They have common size $m\times n$; denote $\ell=mn$. These images will be fused to obtain the binary image $\boldsymbol{I}_F$.

We compare the results of six fusion techniques: simple average, MR-DWT, PCA, ROC statistics, MR-SWT, and MR-SVD.

A. Simple Average

The simple average fusion method proposes the arithmetic mean of the edge evidence in each of the n_c channels: $\boldsymbol{I}_F(x,y)=(n_c)^{-1}\sum_{c=1}^{n_c}\widehat{\boldsymbol{J}}_c(x,y)$, where $1\le x\le m$ indexes the rows, and $1\le y\le n$ the columns of the image.

B. Multiresolution Discrete Wavelet

This section is based on [14]. We apply DWT filters on each binary image $\widehat{\boldsymbol{J}}_c$: a low-pass filter $\boldsymbol{L}$ in the vertical direction, and a high-pass filter $\boldsymbol{H}$ in the horizontal direction, then both are downsampled to create the coefficient matrices $\widehat{\boldsymbol{J}}_{c\mathrm{L}}$ and $\widehat{\boldsymbol{J}}_{c\mathrm{H}}$. These operations are repeated on the coefficient matrices, leading to $\widehat{\boldsymbol{J}}_{c\mathrm{LL}}$, $\widehat{\boldsymbol{J}}_{c\mathrm{LH}}$, $\widehat{\boldsymbol{J}}_{c\mathrm{HL}}$, and $\widehat{\boldsymbol{J}}_{c\mathrm{HH}}$. We, thus, use two resolution levels.

The DWT fusion method has the following steps.

1) Calculate the DWT decomposition $\widehat{\boldsymbol{J}}_{c\mathrm{LL}}$, $\widehat{\boldsymbol{J}}_{c\mathrm{LH}}$, $\widehat{\boldsymbol{J}}_{c\mathrm{HL}}$, and $\widehat{\boldsymbol{J}}_{c\mathrm{HH}}$, for each channel.
2) Compute $\bar{\boldsymbol{J}}_{c\mathrm{HH}}$, the pixel-wise mean of all $\widehat{\boldsymbol{J}}_{c\mathrm{HH}}$ decompositions.
3) Find the pixel-wise maximum of $\widehat{\boldsymbol{J}}_{c\mathrm{LL}}$, $\widehat{\boldsymbol{J}}_{c\mathrm{LH}}$, $\widehat{\boldsymbol{J}}_{c\mathrm{HL}}$: $\bar{\boldsymbol{J}}_{c\mathrm{LL}}$, $\bar{\boldsymbol{J}}_{c\mathrm{LH}}$, and $\bar{\boldsymbol{J}}_{c\mathrm{HL}}$.
4) The result of the fusion I_F is the inverse DWT transform of the coefficient matrices $\bar{\boldsymbol{J}}_{c\mathrm{HH}}$, $\bar{\boldsymbol{J}}_{c\mathrm{LL}}$, $\bar{\boldsymbol{J}}_{c\mathrm{LH}}$, and $\bar{\boldsymbol{J}}_{c\mathrm{HL}}$.

C. Principal Component Analysis

This section is based on [10], [14]. The method comprises of the following steps.

1) Stack the binary images $\widehat{\boldsymbol{J}}_c$ in column vectors to obtain the matrix $\boldsymbol{X}_{\ell \times n_c}$.
2) Calculate the covariance matrix $\boldsymbol{C}_{n_c \times n_c}$ of $\boldsymbol{X}_{\ell \times n_c}$.
3) Compute the matrices of eigenvalues ($\boldsymbol{\Lambda}$) and eigenvectors ($\boldsymbol{V}$) of the covariance matrix, sorted in decreasing order by the eigenvalues.
4) Compute the vector $\boldsymbol{P} = (P(1), \ldots, P(n_c)) = (\sum_{c=1}^{n_c} V(c))^{-1} \boldsymbol{V}$, where $\boldsymbol{V}$ is eigenvector associated with the highest eigenvalue of $\boldsymbol{C}_{n_c \times n_c}$; notice that $\sum_{c=1}^{n_c} P(c) = 1$.
5) Fuse $\boldsymbol{I}_F(x, y) = \sum_{c=1}^{n_c} P(c) \widehat{\boldsymbol{J}}_c(x, y)$.

D. ROC Statistics

The ROC method was proposed and described on [15].

1) Add the binary images $\widehat{\boldsymbol{J}}_c$ to produce the frequency matrix ($\boldsymbol{V}$).
2) Use thresholds ranging from $t = 1, \ldots, n_c$ on $\boldsymbol{V}$ to generate matrices $\boldsymbol{M}_t$.
3) Compare each $\boldsymbol{M}_t$ with all $\widehat{\boldsymbol{J}}_c$, find the confusion matrix to generate the ROC curve. The optimal threshold corresponds to the point of the ROC curve closest (in the sense of the Euclidean distance) to the diagnostic line.
4) The fusion $\boldsymbol{I}_F$ is the matrix $\boldsymbol{M}_t$ which corresponds to the optimal threshold.

E. Multiresolution Stationary Wavelet Transform

This section is based on [14], [16]. The difference between MR-DWT and MR-SWT method is the replacement of the DWT by the SWT.

F. Multiresolution Singular Value Decomposition

MR-SVD fusion [17] works similar to MR-DWT. The MR-SVD fusion method can be summarized as follows.

1) Organize the binary image $\widehat{\boldsymbol{J}}_c$ as nonoverlapping 2×2 blocks, and arrange each block as a 4×1 vector by stacking columns to form the data matrix $\boldsymbol{X}_1$ with dimension $4 \times \ell/4$.
2) Find the SVD decomposition of $\boldsymbol{X}_1 = \boldsymbol{U}_1 \boldsymbol{S}_1 \boldsymbol{V}_1^T$, where $\boldsymbol{U}_1$ is a 4×4 unitary matrix, $\boldsymbol{S}_1$ is a $4 \times \ell/4$ rectangular diagonal matrix known as singular values matrix, and $\boldsymbol{V}_1$ is an $\ell/4 \times \ell/4$ unitary matrix. The singular values are ordered in a decreasing order.
3) Transform the lines of $\widehat{\boldsymbol{X}}_1 = \boldsymbol{U}_1^T \boldsymbol{X}_1 = \boldsymbol{S}_1 \boldsymbol{V}_1^T$ into new matrices with dimensions $m/2 \times n/2$: $\{\boldsymbol{\Phi}_1, \boldsymbol{\Psi}_{1\mathrm{V}}, \boldsymbol{\Psi}_{1\mathrm{H}}, \boldsymbol{\Psi}_{1\mathrm{D}}\}$.
4) Repeat the procedure (1) on $\boldsymbol{\Phi}_r$ by $r = 2$ up to the lowest resolution level R.
5) The MR-SVD decomposition in each channel is

$$\widehat{\boldsymbol{X}}_c \rightarrow \left\{\boldsymbol{\Phi}_{\mathrm{R}}^c, \left\{\boldsymbol{\Psi}_{r\mathrm{V}}^c, \boldsymbol{\Psi}_{r\mathrm{H}}^c, \boldsymbol{\Psi}_{r\mathrm{D}}^c\right\}_{r=1}^{\mathrm{R}}, \left\{\boldsymbol{U}_r^c\right\}_{r=1}^{\mathrm{R}}\right\}.$$

6) Once the decomposition is applied to all channels, compute the average of $\boldsymbol{\Phi}_R^c$ ($\boldsymbol{\Phi}_{\mathrm{R}}^f$) in the lowest resolution level, and the average of $\boldsymbol{U}_r^c$ ($\boldsymbol{U}_{\mathrm{r}}^f$), for each r, where f denotes the fusion among channels.
7) Find the pixel-wise maxima of $\boldsymbol{\Psi}_{r\mathrm{V}}^c$, $\boldsymbol{\Psi}_{r\mathrm{H}}^c$, and $\boldsymbol{\Psi}_{r\mathrm{D}}^c$: $\boldsymbol{\Psi}_{rV}^f$ $\boldsymbol{\Psi}_{r\mathrm{V}}^f$, $\boldsymbol{\Psi}_{r\mathrm{H}}^f$, and $\boldsymbol{\Psi}_{r\mathrm{D}}^f$.
8) The fusion $\boldsymbol{I}_F$ is the SVD transformation for each level $r = \mathrm{R}, \ldots, 1$,

$$\boldsymbol{I}_F \leftarrow \left\{\boldsymbol{\Phi}_{\mathrm{R}}^f, \left\{\boldsymbol{\Psi}_{r\mathrm{V}}^f, \boldsymbol{\Psi}_{r\mathrm{H}}^f, \boldsymbol{\Psi}_{r\mathrm{D}}^f\right\}_{r=\mathrm{R}}^{1}, \left\{\boldsymbol{U}_r^f\right\}_{r=\mathrm{R}}^{1}\right\}.$$

We also used two resolution levels.

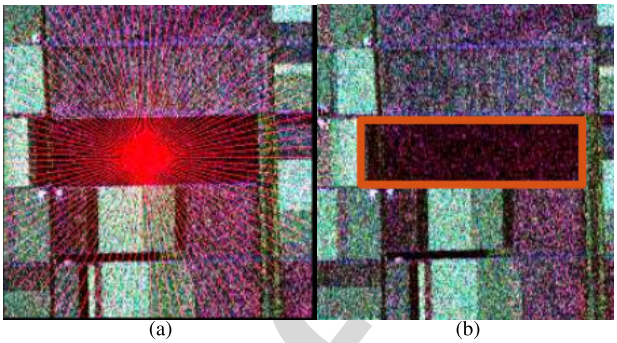

(a) (b)

Fig. 1. Flevoland image in Pauli decomposition, and ground reference. (a) Image and rays. (b) Ground reference.

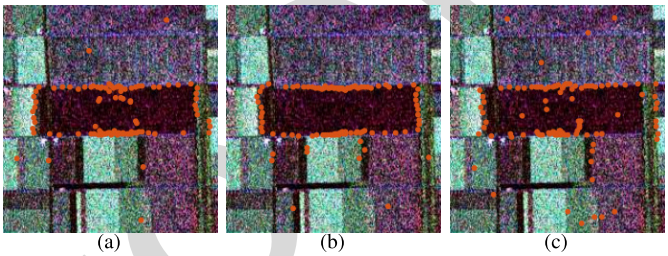

(a) (b) (c)

Fig. 2. Edges evidences from the three intensity channels. (a) Channel hh. (b) Channel hv. (c) Channel vv.

V. Results

A. Flevoland Images

Fig. 1(a) shows a 750 × 1024 pixels AIRSAR PolSAR image of Flevoland, L-band, with the radial lines where edges are detected. Fig. 1(b) shows the ground reference in red.

Fig. 2(a)–(c) shows, respectively, the edge evidences in the hh, hv and vv channels as obtained by MLE.

It is worth noting that GenSA has accurately identified the maximum value of $\mathcal{L}$ [See (4)], even in the presence of multiple local maxima. A visual assessment leads to conclude that the best results are provided by hv, although with a few points far from the actual edge.

Fig. 3(a)–(f) shows the results of fusing these evidences.

Simple average and PCA produce similar results. MR-SVD produces considerably less outliers than the other methods. ROC produces accurate edges, with few outliers, but sparsely. Both wavelet-based methods (DWT and SWT) produce too dense edges and many outliers.

Fig. 4 shows another region in the Flevoland image. In this case, it is a bright target surrounded by darker fields. Fig. 5 shows the edges detected in each intensity channel and, again, the hv data are the one which produce the most accurate results.

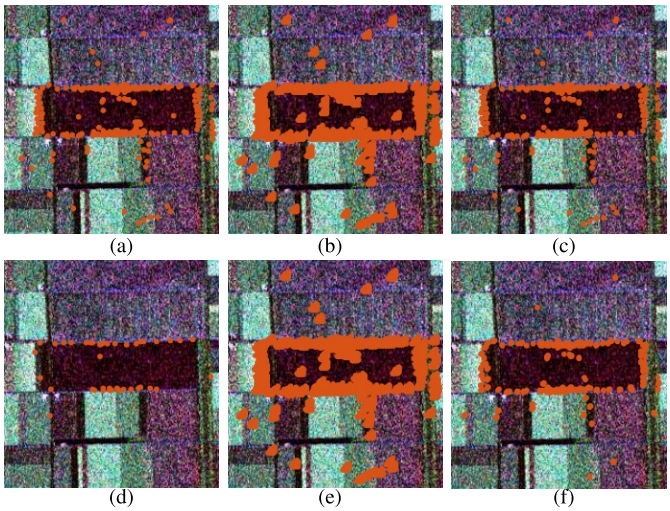

Fig. 3. Results of applying the six fusion methods. (a) Average fusion. (b) MR-DWT fusion. (c) PCA fusion. (d) ROC fusion. (e) MR-SWT fusion. (f) MR-SVD fusion.

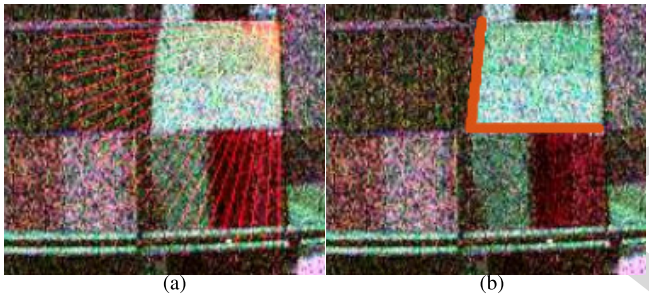

Fig. 4. Flevoland image in Pauli decomposition, and ground reference. (a) Image and rays. (b) Ground reference.

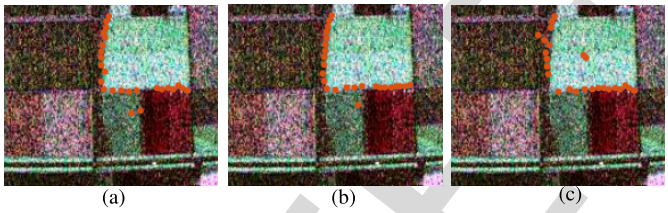

Fig. 5. Edges evidences from the three intensity channels, Flevoland image. (a) Channel hh. (b) Channel hv. (c) Channel vv.

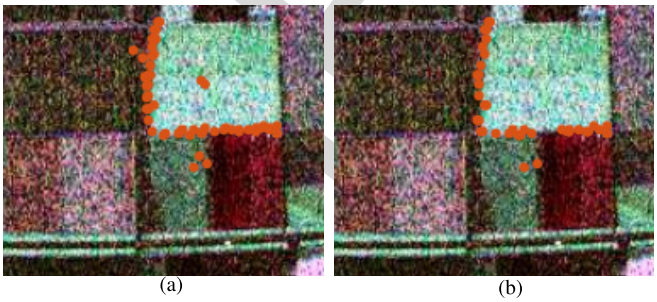

Fig. 6. Two best fusion results in the Flevoland image. (a) PCA fusion. (b) MR-SVD fusion.

Fig. 6 shows the two best fusion results: PCA and MR-SVD. Notice that the latter [Fig. 6(b)] eliminates the wrong detection close to the center of the area and has fewer wrongly detected points outside the region of interest.

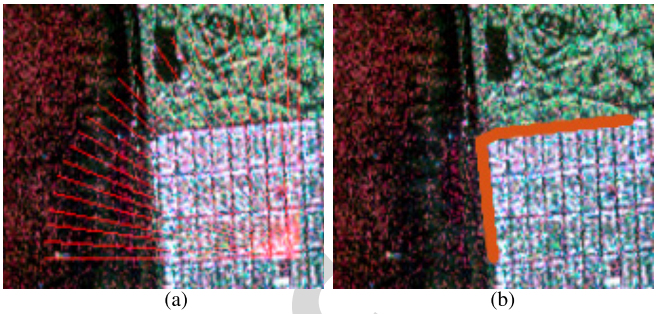

Fig. 7. San Francisco image in Pauli decomposition, and ground reference. (a) Image and rays. (b) Ground reference.

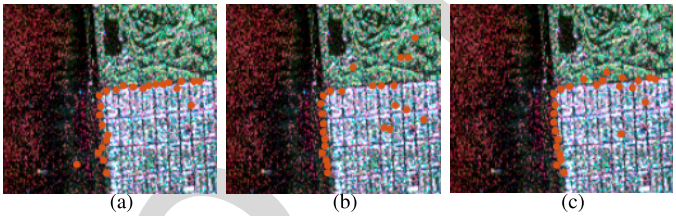

Fig. 8. Edges evidences from the three intensity channels to San Francisco. (a) Channel hh. (b) Channel hv. (c) Channel vv.

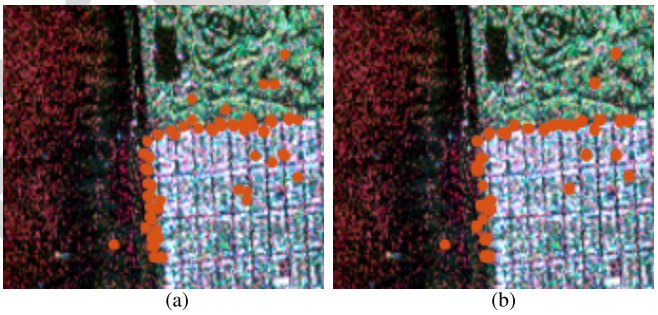

Fig. 9. Two best fusion results in the San Francisco image. (a) PCA fusion. (b) MR-SVD fusion.

B. San Francisco Image

Fig. 7 shows an area of an L-band AIRSAR image over San Francisco. The distinctive areas are urban, sea, and vegetation. The aim is finding the edge between the former and the other two.

Fig. 8 shows the evidences of edges found in each of the three intensity channels. A visual inspection suggests that the hh channel is the one that produces the best estimation.

Fig. 9 shows the two best fusion results: PCA and MR-SVD. Again, the latter is more resistant to outliers, both inside and outside the region of interest.

C. Error Analysis

Fig. 10 shows the error of $\widehat{j}$ in finding the true edge shown in Fig. 1(b), as measured on 100 lines with the minimum Euclidean distance between the ground truth and the detected pixel in the fusion methods. We use relative frequencies to estimate the probability of having an error smaller than a number of pixels. Denoting $H(k)$ the number of lines for which the error is less than k pixels, an estimate of this probability is $f(k) = H(k)/n_r$, where n_r is number of lines.

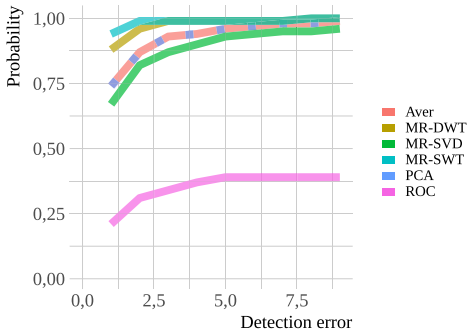

Fig. 10. Probability of detecting the edge by the fusion methods in Fig. 1.

TABLE I
PROCESSING TIMES (FUSION METHOD)

Method	Aver.	PCA	MR-DWT	MR-SWT	ROC	MR-SVD
Time (s)	0.01	0.02	0.08	0.18	0.40	1.11
Rel. time	1.00	2.19	9.25	21.05	46.59	129.57

In our analysis, k varies between 1 and 10, and $n_r = 100$. The algorithm is described in [8].

We obtained similar results on the images shown in Figs. 4 and 7, which we omit for brevity.

D. Implementation Details

Table I shows the running times (absolute and relative to the fastest method). The system presented here was executed on a Intel Core i7-9750HQ CPU 2.6-GHz 16-GB RAM computer.

The method for detecting edge evidence MLE was implemented in the R language. The fusion methods were implemented in MATLAB. Code and data are available at https://github.com/anderborba/Code_GRSL_2020_1.

VI. CONCLUSION

We found evidence of edges using the maximum likelihood method under the Wishart model for PolSAR data. The evidence was found in each of the three intensity channels of AIRSAR L-band images over Flevoland and San Francisco.

Over the agricultural fields of Flevoland, the best edge evidence was observed on the hv channel. The hh channel provided the best estimates of the edges between the urban and both sea and vegetation areas of San Francisco. Such diversity of information content justifies the need of fusing the edge evidences.

We applied simple average, MR-DWT, PCA, ROC, MR-SWT, and MR-SVD fusion methods to aggregate the evidence obtained in the three channels. The best results were produced by PCA and by the MR-SVD. Such enhancement comes at additional computational cost in terms of processing time.

We quantitatively assessed the results by checking the closeness of the fused points to the actual edge, and by the presence of outliers. Although the average and PCA are similar with respect to the probability of correctly detecting the edge, the latter provides a more effective weight of the evidences. In fact, PCA is able to completely discard misleading evidences, while the average cannot.

Two avenues for future improvement of the fusion are: 1) increasing the number of evidences. This is possible, since fully polarimetric data are richer than mere intensity channels; and 2) postprocessing of both partial evidences and fusion.

REFERENCES

[1] J. Shi, H. Jin, and Z. Xiao, "A novel hybrid edge detection method for polarimetric SAR images," *IEEE Access*, vol. 8, pp. 8974–8991, 2020.
[2] B. Liu, Z. Zhang, X. Liu, and W. Yu, "Edge extraction for polarimetric SAR images using degenerate filter with weighted maximum likelihood estimation," *IEEE Geosci. Remote Sens. Lett.*, vol. 11, no. 12, pp. 2140–2144, Dec. 2014.
[3] W. Wang, D. Xiang, Y. Ban, J. Zhang, and J. Wan, "Enhanced edge detection for polarimetric SAR images using a directional span-driven adaptive window," *Int. J. Remote Sens.*, vol. 39, no. 19, pp. 6340–6357, Oct. 2018.
[4] D. Santana-Cedres, L. Gomez, L. Alvarez, and A. C. Frery, "Despeckling PolSAR images with a structure tensor filter," *IEEE Geosci. Remote Sens. Lett.*, vol. 17, no. 2, pp. 357–361, Feb. 2020.
[5] F. Baselice and G. Ferraioli, "Statistical edge detection in urban areas exploiting SAR complex data," *IEEE Geosci. Remote Sens. Lett.*, vol. 9, no. 2, pp. 185–189, Mar. 2012.
[6] X. X. Zhu *et al.*, "Deep learning in remote sensing: A comprehensive review and list of resources," *IEEE Geosci. Remote Sens. Mag.*, vol. 5, no. 4, pp. 8–36, Dec. 2017.
[7] J. Gambini, M. E. Mejail, J. Jacobo-Berlles, and A. C. Frery, "Feature extraction in speckled imagery using dynamic B-spline deformable contours under the model," *Int. J. Remote Sens.*, vol. 27, no. 22, pp. 5037–5059, Nov. 2006.
[8] A. C. Frery, J. Jacobo-Berlles, J. Gambini, and M. E. Mejail, "Polarimetric SAR image segmentation with B-splines and a new statistical model," *Multidimensional Syst. Signal Process.*, vol. 21, no. 4, pp. 319–342, Dec. 2010.
[9] A. D. C. Nascimento, M. M. Horta, A. C. Frery, and R. J. Cintra, "Comparing edge detection methods based on stochastic entropies and distances for PolSAR imagery," *IEEE J. Sel. Topics Appl. Earth Observ. Remote Sens.*, vol. 7, no. 2, pp. 648–663, Feb. 2014.
[10] H. Mitchell, *Image Fusion: Theories, Techniques and Applications*. Berlin, Germany: Springer, 2010.
[11] A. A. de Borba, M. Marengoni, and A. C. Frery, "Fusion of evidences for edge detection in PolSAR images," in *Proc. IEEE Recent Adv. Geosci. Remote Sens., Technol., Standards Appl. (TENGARSS)*, Oct. 2019, pp. 80–85.
[12] J. Gambini, M. E. Mejail, J. Jacobo-Berlles, and A. C. Frery, "Accuracy of edge detection methods with local information in speckled imagery," *Statist. Comput.*, vol. 18, no. 1, pp. 15–26, Mar. 2008.
[13] Y. Xiang, S. Gubian, B. Suomela, and J. Hoeng, "Generalized simulated annealing for global optimization: The GenSA package," *R J.*, vol. 5, no. 1, pp. 13–28, 2013.
[14] V. Naidu and J. Raol, "Pixel-level image fusion using wavelets and principal component analysis," *Defence Sci. J.*, vol. 58, no. 3, pp. 338–352, May 2008.
[15] S. Giannarou and T. Stathaki, "Optimal edge detection using multiple operators for image understanding," *EURASIP J. Adv. Signal Process.*, vol. 2011, no. 1, p. 28, Jul. 2011.
[16] Q. Jiang, X. Jin, S.-J. Lee, and S. Yao, "A novel multi-focus image fusion method based on stationary wavelet transform and local features of fuzzy sets," *IEEE Access*, vol. 5, pp. 20286–20302, 2017.
[17] V. P. S. Naidu, "Image fusion technique using multi-resolution singular value decomposition," *Defence Sci. J.*, vol. 61, no. 5, pp. 479–484, Sep. 2011.
[18] A. Henningsen and O. Toomet, "maxLik: A package for maximum likelihood estimation in R," *Comput. Statist.*, vol. 26, no. 3, pp. 443–458, Sep. 2011.

AUTHOR QUERIES

AUTHOR PLEASE ANSWER ALL QUERIES

PLEASE NOTE: We cannot accept new source files as corrections for your article. If possible, please annotate the PDF proof we have sent you with your corrections and upload it via the Author Gateway. Alternatively, you may send us your corrections in list format. You may also upload revised graphics via the Author Gateway.

Carefully check the page proofs (and coordinate with all authors); additional changes or updates WILL NOT be accepted after the article is published online/print in its final form. Please check author names and affiliations, funding, as well as the overall article for any errors prior to sending in your author proof corrections.

1) **Please be aware that authors are required to pay overlength page charges ($230 per page) if the article is longer than 3 pages. If you cannot pay any or all of these charges please let us know. GRS Society members receive a discounted rate of $200 per page.**

2) **This pdf contains 2 proofs. The first half is the version that will appear on Xplore. The second half is the version that will appear in print. If you have any figures to print in color, they will be in color in both proofs.**

3) **The "Open Access" option for your article expires when the article is published on Xplore in an issue with page numbers. Articles in "Early Access" may be changed to Open Access. If you have not completed your electronic copyright form (ECF) and payment option please return to Scholar One "Transfer Center." In the Transfer Center you will click on "Manuscripts with Decisions" link. You will see your article details and under the "Actions" column click "Transfer Copyright." From the ECF it will direct you to the payment portal to select your payment options and then return to ECF for copyright submission.**

AQ:1 = Please check whether the edit made to the article title is appropriate.
AQ:2 = Please provide the expansions for ROC, BFGS, and AIRSAR.
AQ:3 = Please confirm or add details for any funding or financial support for the research of this article.
AQ:4 = Please confirm whether the corresponding author has been identified correctly.
AQ:5 = Please check and confirm whether the affiliation details of all the authors are correct as set.

Fusion of Evidences in Intensity Channels for Edge Detection in PolSAR Images

Anderson A. De Borba, Maurício Marengoni, and Alejandro C. Frery, *Senior Member, IEEE*

***Abstract*— Polarimetric synthetic aperture radar (PolSAR) sensors have reached an essential position in remote sensing. The images they provide have speckle noise, making their processing and analysis challenging tasks. We discuss an edge detection method based on the fusion of evidences obtained in the intensity channels hh, hv, and vv of PolSAR multilook images. The method consists of detecting transition points in the thinnest possible range of data that covers two regions using maximum likelihood under the Wishart distribution. The fusion methods used are: simple average, multiresolution discrete wavelet transform (MR-DWT), principal component analysis (PCA), ROC statistics, multiresolution stationary wavelet transform (MR-SWT), and a multiresolution method based on singular value decomposition (MR-SVD). A quantitative analysis suggests that PCA and MR-SVD provide the best results.**

***Index Terms*— Edge detection, fusion methods, maximum likelihood estimation, polarimetric synthetic aperture radar (PolSAR).**

I. Introduction

POLARIMETRIC synthetic aperture radar (PolSAR) has achieved an essential position in remote sensing. The data such sensors provide require specifically tailored signal processing techniques. Among such techniques, edge detection is one of the most important operations for extracting information. Edges are at a higher level of abstraction than mere data and, as such, provide relevant insights about the scene.

Among the available edge detection techniques for SAR and PolSAR images, it is worth mentioning: techniques based on denoising [1]–[4]; Markov random fields [5]; the deep learning approach [6] applied to segmentation and classification; and statistical techniques [7]–[9] applied in edge detection in PolSAR and SAR imagery.

This letter follows the statistical modeling approach using the techniques described in [7]–[9] to find edge evidences, followed by fusion processes [10], [11].

Instead of handling fully polarimetric data, we treat each intensity channel separately, obtain evidence of edges, and then produce a single estimator of the edge position. With this, we quantify the contribution each channel provides to the solution of the problem.

The Gambini Algorithm [12] is an attractive edge detection technique. It is local, as it finds evidence of an edge over a thin strip of data; it works with any model, which makes it suitable for SAR data; and it has shown better performance than other approaches. This algorithm consists in casting rays, and then finding the evidence of an edge in the ray by maximizing a value function. We use the total likelihood of two samples: one inside the edge and another outside the edge. Without loss of generality, we assume the complex scaled Wishart distribution for the fully polarimetric observations, from which Gamma laws stem for each intensity channel. The value function depends on the estimates that index such Gamma laws; and we estimate them by maximum likelihood.

The total likelihood function is nondifferentiable at most points, and classical methods have difficulties in finding its maximum. We used the generalized simulated annealing (GenSA) [13] method to solve this problem.

We discuss and compare six fusion methods: Simple average [10], multiresolution discrete wavelet (MR-DWT) [14], principal component analysis (PCA) [10], [14], ROC statistics [15], multiresolution stationary wavelet transform (MR-SWT) [14], [16], and multiresolution singular value decomposition (MR-SVD) [17].

The letter is structured as follows: Section II describes the models, Section III describes the edge detection, Section IV describes the approaches for fusing edge evidences, Section V presents the results, and in Section VI we discuss the results and outline future research directions.

II. Statistical Modeling for PolSAR Data

Multilooked fully polarimetric data follow the Wishart distribution with probability density function (PDF) defined by:

$$f_{\mathbf{Z}}(\mathbf{z};\,\Sigma,\,L)=\frac{L^{pL}|\mathbf{z}|^{L-p}}{|\Sigma|^{L}\Gamma_p(L)}\exp(-L\,\mathrm{tr}(\Sigma^{-1}\mathbf{z})) \qquad (1)$$

where $\mathbf{z}$ is a positive-definite Hermitian matrix, L is the number of looks, $\mathrm{tr}(\cdot)$ is the trace operator of a matrix, $\Gamma_p(L)$ is the multivariate Gamma function defined by $\Gamma_p(L) = \pi^{1/2p(p-1)}\prod_{i=0}^{p-1}\Gamma(L-i)$, and $\Gamma(\cdot)$ is the Gamma function. We used three $p=3$ channels in this study. This situation is denoted by $\mathbf{Z}\sim W(\Sigma,L)$, which satisfies $E[\mathbf{Z}]=\Sigma$. This assumption usually holds for fully developed speckle but, since we will estimate L locally instead of considering the same number of looks for the whole image, we will in part take into account departures from such hypothesis.

Manuscript received March 24, 2020; revised July 12, 2020; accepted August 31, 2020. *(Corresponding author: Anderson A. De Borba.)*

Anderson A. De Borba is with the Department of Engenharia Elétrica e Computação, Universidade Presbiteriana Mackenzie (UPM), São Paulo 01302-907, Brazil, and also with IBMEC-SP, São Paulo 01419-002, Brazil (e-mail: anderson.aborba@professores.ibmec.edu.br).

Maurício Marengoni is with the Department of Engenharia Elétrica e Computação, Universidade Presbiteriana Mackenzie (UPM), São Paulo 01302-907, Brazil (e-mail: mauricio.marengoni@mackenzie.br).

Alejandro C. Frery is with the School of Mathematics and Statistics, Victoria University of Wellington, Wellington 6140, New Zealand (e-mail: alejandro.frery@vuw.ac.nz).

Color versions of one or more of the figures in this letter are available online at http://ieeexplore.ieee.org.

Digital Object Identifier 10.1109/LGRS.2020.3022511

Since we are interested in describing the information conveyed by parts of such matrix under the Wishart model, we assume that the distribution of each intensity channel is a Gamma law with PDF

$$f_Z(z;\mu,L)=\frac{L^L z^{L-1}}{\mu^L\Gamma(L)}\exp\{-Lz/\mu\},\quad z>0 \tag{2}$$

where $L>0$, and $\mu>0$ is the mean. The log-likelihood of the sample $\boldsymbol{z}=(z_1,\ldots,z_n)$ under this model is

$$\mathcal{L}(\mu,L;\boldsymbol{z})=n[L\ln(L/\mu)-\ln\Gamma(L)] +L\sum_{k=1}^{n}\ln z_k-\frac{L}{\mu}\sum_{k=1}^{n}z_k. \tag{3}$$

We obtain $(\widehat{\mu},\widehat{L})$, the maximum likelihood estimator (MLE) of (μ,L) based on $\boldsymbol{z}$, by maximizing (3) with the BFGS method [18]. We prefer optimization to solving $\nabla\ell=\mathbf{0}$ for improved numerical stability.

III. Edge Detection on a Single Data Strip

The Gambini algorithm estimates the point at which the properties of a sample change. It has been used with stochastic distances [9] and with the likelihood function [7], [8] for edge detection in SAR/PolSAR imagery. It can be adapted to any suitable measure of dissimilarity between two samples.

The algorithm starts by casting rays from a point inside the candidate region, e.g., the centroid. Data are collected around each ray to form the sample $\boldsymbol{z}=(z_1,z_2,\ldots,z_n)$, which is partitioned at position j

$$\boldsymbol{z}=(\underbrace{z_1,z_2,\ldots,z_j}_{\boldsymbol{z}_\mathrm{I}},\ \underbrace{z_{j+1},z_{j+2},\ldots,z_n}_{\boldsymbol{z}_\mathrm{E}}).$$

We assume two (possibly) different models for each partition: $\boldsymbol{Z}_\mathrm{I}\sim\Gamma(\mu_\mathrm{I},L_\mathrm{I})$, and $\boldsymbol{Z}_\mathrm{E}\sim\Gamma(\mu_\mathrm{E},L_\mathrm{E})$. We then estimate $(\mu_\mathrm{I},L_\mathrm{I})$ and $(\mu_\mathrm{E},L_\mathrm{E})$ with $\boldsymbol{z}_\mathrm{I}$ and $\boldsymbol{z}_\mathrm{E}$, respectively, by maximizing (3), and obtain $(\widehat{\mu}_\mathrm{I},\widehat{L}_\mathrm{I})$ and $(\widehat{\mu}_\mathrm{E},\widehat{L}_\mathrm{E})$.

We then compute the total log-likelihood of $\boldsymbol{z}_\mathrm{I}$ and $\boldsymbol{z}_\mathrm{E}$

$$\begin{aligned}\mathcal{L}(j;\widehat{\mu}_I,\widehat{L}_I,\widehat{\mu}_E,\widehat{L}_E)&=-\left(\frac{\widehat{L}_\mathrm{I}}{\widehat{\mu}_\mathrm{I}}\sum_{k=1}^{j}z_k+\frac{\widehat{L}_\mathrm{E}}{\widehat{\mu}_\mathrm{E}}\sum_{k=j+1}^{n}z_k\right)\\&\quad+j[\widehat{L}_\mathrm{I}\ln(\widehat{L}_\mathrm{I}/\widehat{\mu}_\mathrm{I})-\ln\Gamma(\widehat{L}_\mathrm{I})]+\widehat{L}_\mathrm{I}\sum_{k=1}^{j}\ln z_k\\&\quad+(n-j)[\widehat{L}_\mathrm{E}\ln(\widehat{L}_\mathrm{E}/\widehat{\mu}_\mathrm{E})-\ln\Gamma(\widehat{L}_\mathrm{E})]+\widehat{L}_\mathrm{E}\sum_{k=j+1}^{n}\ln z_k.\end{aligned} \tag{4}$$

and the estimate of the edge position on the ray is the coordinate $\widehat{j}$ which maximizes it.

Algorithm 1 is the pseudocode of the basic edge detection with the Gambini Algorithm. We found that 100 rays is a good compromise between spatial continuity and computational load. Also, $\min_s$ is the minimum sample size.

In our implementation, we replace the exhaustive sequential search (the innermost **for** loop) by GenSA [13].

Algorithm 1 Gambini Algorithm for Intensity Channels

Data: n_c intensity channels, interior point, number of rays
Result: n_c binary images with evidences of edges
for *each band* $1\le c\le n_c$ **do**
  for *each ray passing through the interior point* **do**
    $\boldsymbol{z}=(z_1,z_2,\ldots,z_n)\leftarrow$ data collected around the ray;
    for *each* $\min_s\le j\le n-\min_s$ **do**
      Partition the sample as $\boldsymbol{z}_\mathrm{I}=(z_{\min_s},\ldots,z_j)$ and $\boldsymbol{z}_\mathrm{E}=(z_{j+1},\ldots,z_{n-\min_s})$;
      Compute $(\widehat{\mu}_\mathrm{I},\widehat{L}_\mathrm{I})$ with $\boldsymbol{z}_\mathrm{I}$, and $(\widehat{\mu}_\mathrm{E},\widehat{L}_\mathrm{E})$ with $\boldsymbol{z}_\mathrm{E}$;
      Compute the total log-likelihood at j as $\mathcal{L}(j;\widehat{\mu}_I,\widehat{L}_I,\widehat{\mu}_E,\widehat{L}_E)$;
    end
    $\widehat{j}\leftarrow$ the value of j which maximizes the total log-likelihood function;
    return $(\widehat{x},\widehat{y})$, the coordinates of each $\widehat{j}$;
  end
  return the binary image $\widehat{\boldsymbol{J}}_c$ with 1 at every $(\widehat{x},\widehat{y})$, and 0 otherwise.
end

IV. Fusion of Evidences

Assume we have n_c binary images $\{\widehat{\boldsymbol{J}}_c\}_{1\le c\le n_c}$ in which 1 denotes an estimate of edge and 0 otherwise. They have common size $m\times n$; denote $\ell=mn$. These images will be fused to obtain the binary image $\boldsymbol{I}_F$.

We compare the results of six fusion techniques: simple average, MR-DWT, PCA, ROC statistics, MR-SWT, and MR-SVD.

A. Simple Average

The simple average fusion method proposes the arithmetic mean of the edge evidence in each of the n_c channels: $\boldsymbol{I}_F(x,y)=(n_c)^{-1}\sum_{c=1}^{n_c}\widehat{\boldsymbol{J}}_c(x,y)$, where $1\le x\le m$ indexes the rows, and $1\le y\le n$ the columns of the image.

B. Multiresolution Discrete Wavelet

This section is based on [14]. We apply DWT filters on each binary image $\widehat{\boldsymbol{J}}_c$: a low-pass filter $\boldsymbol{L}$ in the vertical direction, and a high-pass filter $\boldsymbol{H}$ in the horizontal direction, then both are downsampled to create the coefficient matrices $\widehat{\boldsymbol{J}}_{c\mathrm{L}}$ and $\widehat{\boldsymbol{J}}_{c\mathrm{H}}$. These operations are repeated on the coefficient matrices, leading to $\widehat{\boldsymbol{J}}_{c\mathrm{LL}}$, $\widehat{\boldsymbol{J}}_{c\mathrm{LH}}$, $\widehat{\boldsymbol{J}}_{c\mathrm{HL}}$, and $\widehat{\boldsymbol{J}}_{c\mathrm{HH}}$. We, thus, use two resolution levels.

The DWT fusion method has the following steps.

1) Calculate the DWT decomposition $\widehat{\boldsymbol{J}}_{c\mathrm{LL}}$, $\widehat{\boldsymbol{J}}_{c\mathrm{LH}}$, $\widehat{\boldsymbol{J}}_{c\mathrm{HL}}$, and $\widehat{\boldsymbol{J}}_{c\mathrm{HH}}$, for each channel.
2) Compute $\bar{\boldsymbol{J}}_{c\mathrm{HH}}$, the pixel-wise mean of all $\widehat{\boldsymbol{J}}_{c\mathrm{HH}}$ decompositions.
3) Find the pixel-wise maximum of $\widehat{\boldsymbol{J}}_{c\mathrm{LL}}$, $\widehat{\boldsymbol{J}}_{c\mathrm{LH}}$, $\widehat{\boldsymbol{J}}_{c\mathrm{HL}}$: $\bar{\boldsymbol{J}}_{c\mathrm{LL}}$, $\bar{\boldsymbol{J}}_{c\mathrm{LH}}$, and $\bar{\boldsymbol{J}}_{c\mathrm{HL}}$.
4) The result of the fusion I_F is the inverse DWT transform of the coefficient matrices $\bar{\boldsymbol{J}}_{c\mathrm{HH}}$, $\bar{\boldsymbol{J}}_{c\mathrm{LL}}$, $\bar{\boldsymbol{J}}_{c\mathrm{LH}}$, and $\bar{\boldsymbol{J}}_{c\mathrm{HL}}$.

C. Principal Component Analysis

This section is based on [10], [14]. The method comprises of the following steps.

1) Stack the binary images $\widehat{\boldsymbol{J}}_c$ in column vectors to obtain the matrix $\boldsymbol{X}_{\ell \times n_c}$.
2) Calculate the covariance matrix $\boldsymbol{C}_{n_c \times n_c}$ of $\boldsymbol{X}_{\ell \times n_c}$.
3) Compute the matrices of eigenvalues ($\boldsymbol{\Lambda}$) and eigenvectors ($\boldsymbol{V}$) of the covariance matrix, sorted in decreasing order by the eigenvalues.
4) Compute the vector $\boldsymbol{P} = (P(1), \ldots, P(n_c)) = (\sum_{c=1}^{n_c} V(c))^{-1} \boldsymbol{V}$, where $\boldsymbol{V}$ is eigenvector associated with the highest eigenvalue of $\boldsymbol{C}_{n_c \times n_c}$; notice that $\sum_{c=1}^{n_c} P(c) = 1$.
5) Fuse $\boldsymbol{I}_F(x, y) = \sum_{c=1}^{n_c} P(c) \widehat{\boldsymbol{J}}_c(x, y)$.

D. ROC Statistics

The ROC method was proposed and described on [15].

1) Add the binary images $\widehat{\boldsymbol{J}}_c$ to produce the frequency matrix ($\boldsymbol{V}$).
2) Use thresholds ranging from $t = 1, \ldots, n_c$ on $\boldsymbol{V}$ to generate matrices $\boldsymbol{M}_t$.
3) Compare each $\boldsymbol{M}_t$ with all $\widehat{\boldsymbol{J}}_c$, find the confusion matrix to generate the ROC curve. The optimal threshold corresponds to the point of the ROC curve closest (in the sense of the Euclidean distance) to the diagnostic line.
4) The fusion $\boldsymbol{I}_F$ is the matrix $\boldsymbol{M}_t$ which corresponds to the optimal threshold.

E. Multiresolution Stationary Wavelet Transform

This section is based on [14], [16]. The difference between MR-DWT and MR-SWT method is the replacement of the DWT by the SWT.

F. Multiresolution Singular Value Decomposition

MR-SVD fusion [17] works similar to MR-DWT. The MR-SVD fusion method can be summarized as follows.

1) Organize the binary image $\widehat{\boldsymbol{J}}_c$ as nonoverlapping 2×2 blocks, and arrange each block as a 4×1 vector by stacking columns to form the data matrix $\boldsymbol{X}_1$ with dimension $4 \times \ell/4$.
2) Find the SVD decomposition of $\boldsymbol{X}_1 = \boldsymbol{U}_1 \boldsymbol{S}_1 \boldsymbol{V}_1^T$, where $\boldsymbol{U}_1$ is a 4×4 unitary matrix, $\boldsymbol{S}_1$ is a $4 \times \ell/4$ rectangular diagonal matrix known as singular values matrix, and $\boldsymbol{V}_1$ is an $\ell/4 \times \ell/4$ unitary matrix. The singular values are ordered in a decreasing order.
3) Transform the lines of $\widehat{\boldsymbol{X}}_1 = \boldsymbol{U}_1^T \boldsymbol{X}_1 = \boldsymbol{S}_1 \boldsymbol{V}_1^T$ into new matrices with dimensions $m/2 \times n/2$: $\{\boldsymbol{\Phi}_1, \boldsymbol{\Psi}_{1\mathrm{V}}, \boldsymbol{\Psi}_{1\mathrm{H}}, \boldsymbol{\Psi}_{1\mathrm{D}}\}$.
4) Repeat the procedure (1) on $\boldsymbol{\Phi}_r$ by $r = 2$ up to the lowest resolution level R.
5) The MR-SVD decomposition in each channel is

$$\widehat{\boldsymbol{X}}_c \rightarrow \left\{\boldsymbol{\Phi}_{\mathrm{R}}^c, \left\{\boldsymbol{\Psi}_{r\mathrm{V}}^c, \boldsymbol{\Psi}_{r\mathrm{H}}^c, \boldsymbol{\Psi}_{r\mathrm{D}}^c\right\}_{r=1}^{\mathrm{R}}, \left\{\boldsymbol{U}_r^c\right\}_{r=1}^{\mathrm{R}}\right\}.$$

6) Once the decomposition is applied to all channels, compute the average of $\boldsymbol{\Phi}_R^c$ ($\boldsymbol{\Phi}_{\mathrm{R}}^f$) in the lowest resolution level, and the average of $\boldsymbol{U}_r^c$ ($\boldsymbol{U}_{\mathrm{r}}^f$), for each r, where f denotes the fusion among channels.
7) Find the pixel-wise maxima of $\boldsymbol{\Psi}_{r\mathrm{V}}^c$, $\boldsymbol{\Psi}_{r\mathrm{H}}^c$, and $\boldsymbol{\Psi}_{r\mathrm{D}}^c$: $\boldsymbol{\Psi}_{rV}^f$ $\boldsymbol{\Psi}_{r\mathrm{V}}^f$, $\boldsymbol{\Psi}_{r\mathrm{H}}^f$, and $\boldsymbol{\Psi}_{r\mathrm{D}}^f$.
8) The fusion $\boldsymbol{I}_F$ is the SVD transformation for each level $r = \mathrm{R}, \ldots, 1$,

$$\boldsymbol{I}_F \leftarrow \left\{\boldsymbol{\Phi}_{\mathrm{R}}^f, \left\{\boldsymbol{\Psi}_{r\mathrm{V}}^f, \boldsymbol{\Psi}_{r\mathrm{H}}^f, \boldsymbol{\Psi}_{r\mathrm{D}}^f\right\}_{r=\mathrm{R}}^{1}, \left\{\boldsymbol{U}_r^f\right\}_{r=\mathrm{R}}^{1}\right\}.$$

We also used two resolution levels.

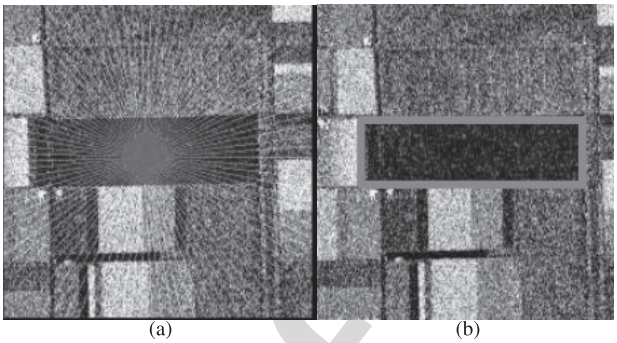

Fig. 1. Flevoland image in Pauli decomposition, and ground reference. (a) Image and rays. (b) Ground reference.

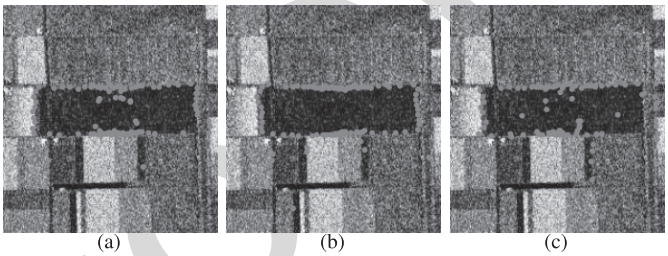

Fig. 2. Edges evidences from the three intensity channels. (a) Channel hh. (b) Channel hv. (c) Channel vv.

V. Results

A. Flevoland Images

Fig. 1(a) shows a 750 × 1024 pixels AIRSAR PolSAR image of Flevoland, L-band, with the radial lines where edges are detected. Fig. 1(b) shows the ground reference in red.

Fig. 2(a)–(c) shows, respectively, the edge evidences in the hh, hv and vv channels as obtained by MLE.

It is worth noting that GenSA has accurately identified the maximum value of $\mathcal{L}$ [See (4)], even in the presence of multiple local maxima. A visual assessment leads to conclude that the best results are provided by hv, although with a few points far from the actual edge.

Fig. 3(a)–(f) shows the results of fusing these evidences.

Simple average and PCA produce similar results. MR-SVD produces considerably less outliers than the other methods. ROC produces accurate edges, with few outliers, but sparsely. Both wavelet-based methods (DWT and SWT) produce too dense edges and many outliers.

Fig. 4 shows another region in the Flevoland image. In this case, it is a bright target surrounded by darker fields. Fig. 5 shows the edges detected in each intensity channel and, again, the hv data are the one which produce the most accurate results.

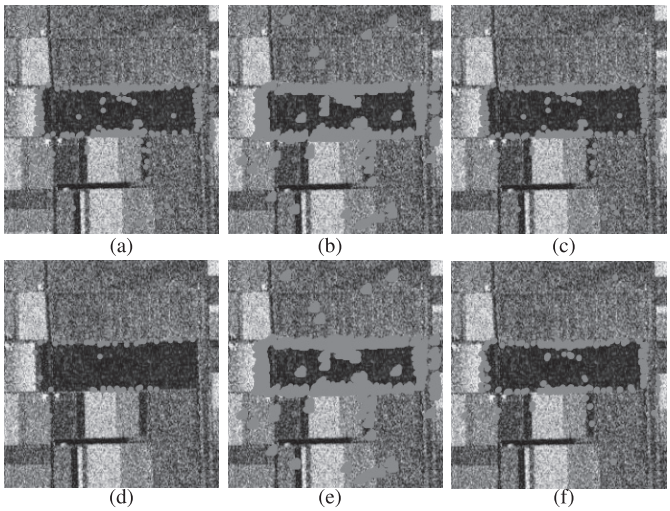

Fig. 3. Results of applying the six fusion methods. (a) Average fusion. (b) MR-DWT fusion. (c) PCA fusion. (d) ROC fusion. (e) MR-SWT fusion. (f) MR-SVD fusion.

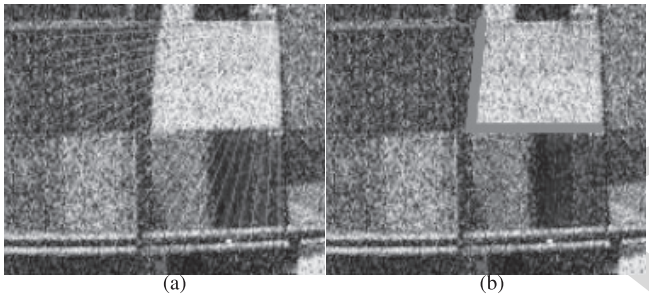

Fig. 4. Flevoland image in Pauli decomposition, and ground reference. (a) Image and rays. (b) Ground reference.

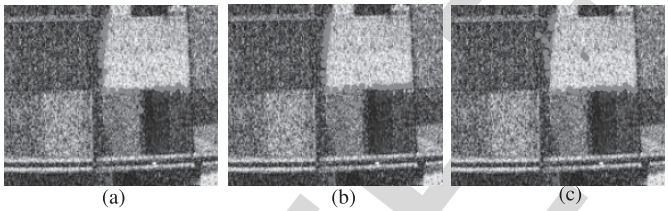

Fig. 5. Edges evidences from the three intensity channels, Flevoland image. (a) Channel hh. (b) Channel hv. (c) Channel vv.

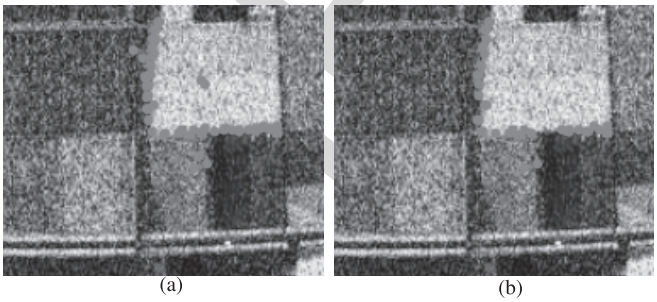

Fig. 6. Two best fusion results in the Flevoland image. (a) PCA fusion. (b) MR-SVD fusion.

Fig. 6 shows the two best fusion results: PCA and MR-SVD. Notice that the latter [Fig. 6(b)] eliminates the wrong detection close to the center of the area and has fewer wrongly detected points outside the region of interest.

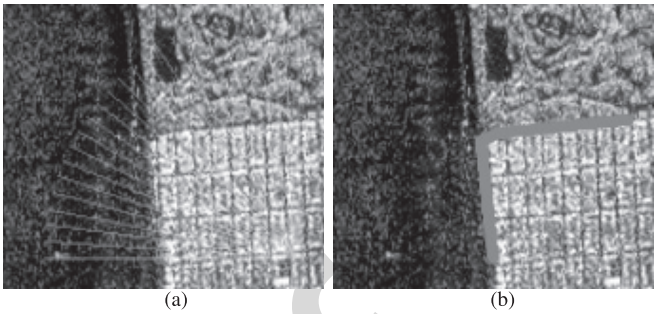

Fig. 7. San Francisco image in Pauli decomposition, and ground reference. (a) Image and rays. (b) Ground reference.

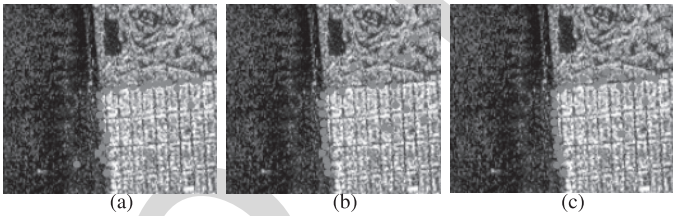

Fig. 8. Edges evidences from the three intensity channels to San Francisco. (a) Channel hh. (b) Channel hv. (c) Channel vv.

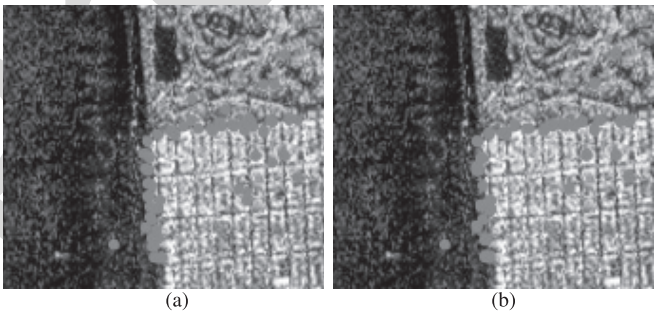

Fig. 9. Two best fusion results in the San Francisco image. (a) PCA fusion. (b) MR-SVD fusion.

B. San Francisco Image

Fig. 7 shows an area of an L-band AIRSAR image over San Francisco. The distinctive areas are urban, sea, and vegetation. The aim is finding the edge between the former and the other two.

Fig. 8 shows the evidences of edges found in each of the three intensity channels. A visual inspection suggests that the hh channel is the one that produces the best estimation.

Fig. 9 shows the two best fusion results: PCA and MR-SVD. Again, the latter is more resistant to outliers, both inside and outside the region of interest.

C. Error Analysis

Fig. 10 shows the error of $\hat{j}$ in finding the true edge shown in Fig. 1(b), as measured on 100 lines with the minimum Euclidean distance between the ground truth and the detected pixel in the fusion methods. We use relative frequencies to estimate the probability of having an error smaller than a number of pixels. Denoting $H(k)$ the number of lines for which the error is less than k pixels, an estimate of this probability is $f(k) = H(k)/n_r$, where n_r is number of lines.

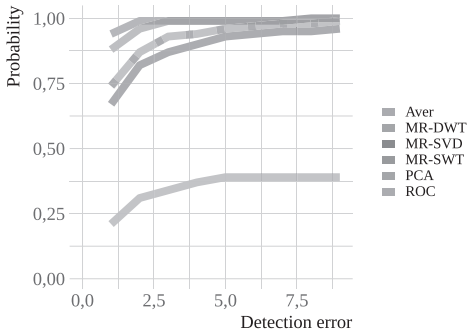

Fig. 10. Probability of detecting the edge by the fusion methods in Fig. 1.

TABLE I
PROCESSING TIMES (FUSION METHOD)

Method	Aver.	PCA	MR-DWT	MR-SWT	ROC	MR-SVD
Time (s)	0.01	0.02	0.08	0.18	0.40	1.11
Rel. time	1.00	2.19	9.25	21.05	46.59	129.57

In our analysis, k varies between 1 and 10, and $n_r = 100$. The algorithm is described in [8].

We obtained similar results on the images shown in Figs. 4 and 7, which we omit for brevity.

D. Implementation Details

Table I shows the running times (absolute and relative to the fastest method). The system presented here was executed on a Intel Core i7-9750HQ CPU 2.6-GHz 16-GB RAM computer.

The method for detecting edge evidence MLE was implemented in the R language. The fusion methods were implemented in MATLAB. Code and data are available at https://github.com/anderborba/Code_GRSL_2020_1.

VI. CONCLUSION

We found evidence of edges using the maximum likelihood method under the Wishart model for PolSAR data. The evidence was found in each of the three intensity channels of AIRSAR L-band images over Flevoland and San Francisco.

Over the agricultural fields of Flevoland, the best edge evidence was observed on the hv channel. The hh channel provided the best estimates of the edges between the urban and both sea and vegetation areas of San Francisco. Such diversity of information content justifies the need of fusing the edge evidences.

We applied simple average, MR-DWT, PCA, ROC, MR-SWT, and MR-SVD fusion methods to aggregate the evidence obtained in the three channels. The best results were produced by PCA and by the MR-SVD. Such enhancement comes at additional computational cost in terms of processing time.

We quantitatively assessed the results by checking the closeness of the fused points to the actual edge, and by the presence of outliers. Although the average and PCA are similar with respect to the probability of correctly detecting the edge, the latter provides a more effective weight of the evidences. In fact, PCA is able to completely discard misleading evidences, while the average cannot.

Two avenues for future improvement of the fusion are: 1) increasing the number of evidences. This is possible, since fully polarimetric data are richer than mere intensity channels; and 2) postprocessing of both partial evidences and fusion.

REFERENCES

[1] J. Shi, H. Jin, and Z. Xiao, "A novel hybrid edge detection method for polarimetric SAR images," *IEEE Access*, vol. 8, pp. 8974–8991, 2020.
[2] B. Liu, Z. Zhang, X. Liu, and W. Yu, "Edge extraction for polarimetric SAR images using degenerate filter with weighted maximum likelihood estimation," *IEEE Geosci. Remote Sens. Lett.*, vol. 11, no. 12, pp. 2140–2144, Dec. 2014.
[3] W. Wang, D. Xiang, Y. Ban, J. Zhang, and J. Wan, "Enhanced edge detection for polarimetric SAR images using a directional span-driven adaptive window," *Int. J. Remote Sens.*, vol. 39, no. 19, pp. 6340–6357, Oct. 2018.
[4] D. Santana-Cedres, L. Gomez, L. Alvarez, and A. C. Frery, "Despeckling PolSAR images with a structure tensor filter," *IEEE Geosci. Remote Sens. Lett.*, vol. 17, no. 2, pp. 357–361, Feb. 2020.
[5] F. Baselice and G. Ferraioli, "Statistical edge detection in urban areas exploiting SAR complex data," *IEEE Geosci. Remote Sens. Lett.*, vol. 9, no. 2, pp. 185–189, Mar. 2012.
[6] X. X. Zhu *et al.*, "Deep learning in remote sensing: A comprehensive review and list of resources," *IEEE Geosci. Remote Sens. Mag.*, vol. 5, no. 4, pp. 8–36, Dec. 2017.
[7] J. Gambini, M. E. Mejail, J. Jacobo-Berlles, and A. C. Frery, "Feature extraction in speckled imagery using dynamic B-spline deformable contours under the model," *Int. J. Remote Sens.*, vol. 27, no. 22, pp. 5037–5059, Nov. 2006.
[8] A. C. Frery, J. Jacobo-Berlles, J. Gambini, and M. E. Mejail, "Polarimetric SAR image segmentation with B-splines and a new statistical model," *Multidimensional Syst. Signal Process.*, vol. 21, no. 4, pp. 319–342, Dec. 2010.
[9] A. D. C. Nascimento, M. M. Horta, A. C. Frery, and R. J. Cintra, "Comparing edge detection methods based on stochastic entropies and distances for PolSAR imagery," *IEEE J. Sel. Topics Appl. Earth Observ. Remote Sens.*, vol. 7, no. 2, pp. 648–663, Feb. 2014.
[10] H. Mitchell, *Image Fusion: Theories, Techniques and Applications*. Berlin, Germany: Springer, 2010.
[11] A. A. de Borba, M. Marengoni, and A. C. Frery, "Fusion of evidences for edge detection in PolSAR images," in *Proc. IEEE Recent Adv. Geosci. Remote Sens., Technol., Standards Appl. (TENGARSS)*, Oct. 2019, pp. 80–85.
[12] J. Gambini, M. E. Mejail, J. Jacobo-Berlles, and A. C. Frery, "Accuracy of edge detection methods with local information in speckled imagery," *Statist. Comput.*, vol. 18, no. 1, pp. 15–26, Mar. 2008.
[13] Y. Xiang, S. Gubian, B. Suomela, and J. Hoeng, "Generalized simulated annealing for global optimization: The GenSA package," *R J.*, vol. 5, no. 1, pp. 13–28, 2013.
[14] V. Naidu and J. Raol, "Pixel-level image fusion using wavelets and principal component analysis," *Defence Sci. J.*, vol. 58, no. 3, pp. 338–352, May 2008.
[15] S. Giannarou and T. Stathaki, "Optimal edge detection using multiple operators for image understanding," *EURASIP J. Adv. Signal Process.*, vol. 2011, no. 1, p. 28, Jul. 2011.
[16] Q. Jiang, X. Jin, S.-J. Lee, and S. Yao, "A novel multi-focus image fusion method based on stationary wavelet transform and local features of fuzzy sets," *IEEE Access*, vol. 5, pp. 20286–20302, 2017.
[17] V. P. S. Naidu, "Image fusion technique using multi-resolution singular value decomposition," *Defence Sci. J.*, vol. 61, no. 5, pp. 479–484, Sep. 2011.
[18] A. Henningsen and O. Toomet, "maxLik: A package for maximum likelihood estimation in R," *Comput. Statist.*, vol. 26, no. 3, pp. 443–458, Sep. 2011.